

## Plentiful abutting functional groups boosting sodium storage in a small molecule

Chenyang Zhang<sup>‡<sup>a</sup></sup>, Cheng Fu<sup>‡<sup>b</sup></sup>, Haoyu Guo<sup>‡<sup>a</sup></sup>, Yuan Chen<sup>a,c</sup>, Kun Fan<sup>a,c</sup>, Zengyu Li<sup>a</sup>,  
Jincheng Zou<sup>a</sup>, Huichao Dai<sup>a</sup>, Guoqun Zhang<sup>a</sup>, Jing Ma<sup>\*<sup>b</sup></sup> and Chengliang Wang<sup>\*<sup>a,c</sup></sup>

<sup>a</sup> School of Integrated Circuits, Wuhan National Laboratory for Optoelectronics (WNLO),  
Key Laboratory of Material Chemistry for Energy Conversion and Storage, Huazhong  
University of Science and Technology, Wuhan 430074, China. E-mail: [clwang@hust.edu.cn](mailto:clwang@hust.edu.cn).

<sup>b</sup> School of Chemistry and Chemical Engineering, Nanjing University, Nanjing 210093,  
China. E-mail: [majing@nju.edu.cn](mailto:majing@nju.edu.cn). <sup>c</sup> Wenzhou Key Laboratory of Optoelectronic Materials  
and Devices Application, Wenzhou Advanced Manufacturing Institute, Huazhong University  
of Science and Technology, Wenzhou 325035, China.

‡ These authors contributed equally to this work.

## Experimental Procedures

### Materials

All starting materials and solvents were purchased from Energy Chemical or Sinopharm Chemical Reagent Co., Ltd and used as received without further purification. 2,3,5,6-tetraamino-1,4-benzoquinone (TABQ) was synthesized through a two-step reaction according to the previous works<sup>1-3</sup>.

### Synthesis of QAPs

QAPs was synthesized according to a previous report with some modifications<sup>4</sup>. TABQ (0.84 g, 5 mmol) and 2,5-dihydroxy-1,4-benzoquinone (DHBQ, 0.7 g, 5 mmol) were charged in the flask bottom, and then 20 mL of glacial acetic acid was slowly added. After stirring 30 min at room temperature, the mixture was heated to 120 °C and maintained 24 h. The resulting dark suspension was filtered and washed several times with deionized water and methanol, and then dried under vacuum at 100 °C for 10 h. Finally, the QAPs powder was collected with a high yield of 92%. <sup>1</sup>H NMR (400 MHz, DMSO-*d*<sub>6</sub>): δ 5.92 (s, 4H) 7.32 (s, 2H) 10.87 (s, 2H); <sup>13</sup>C NMR (400 MHz, DMSO-*d*<sub>6</sub>): δ 176.07, δ 153.09, δ 142.07, δ 139.44, δ 130.75, δ 110.95; HR-MS (m/z): (M-H)<sup>-</sup> calcd For C<sub>12</sub>H<sub>7</sub>N<sub>4</sub>O<sub>4</sub><sup>-</sup> 271.04724; found, 271.04730.

### Synthesis of QAPs\_2Na\_syn

The QAPs\_2Na\_syn was prepared through an acid-base neutralization reaction. 272 mg (1 mmol) of QAPs was dispersed into 20 mL deionized water, and then 80 mg (2 mmol) of sodium hydroxide was added to the above solution, followed by raising the reaction temperature to 80 °C for 10 h. After cooling to room temperature, a number of black precipitates were precipitated by adding the poor solvent ethyl alcohol. The precipitates were collected by centrifugation and washed several times with absolute ethyl alcohol, and dried under vacuum at 80 °C for 10 h. Finally, the black QAPs\_2Na\_syn powder was obtained. Calcd elemental analysis (%) for the QAPs\_Na (Na<sub>2</sub>C<sub>12</sub>H<sub>6</sub>N<sub>4</sub>O<sub>4</sub>·2.5H<sub>2</sub>O·0.2NaOH): Na 13.70, C 39.04, H 3.06, N 15.17, O 29.03; found: Na 13.48, C 39.30, H 2.39, N 15.20, O 29.63.

### Characterizations

$^1\text{H}$  nuclear magnetic resonance (NMR) and  $^{13}\text{C}$  NMR spectra were recorded on a Bruker Avance 400 (400 MHz) spectrometer, using  $\text{DMSO-}d_6$  as solvent and tetramethylsilane (TMS) as internal standard. Liquid chromatography high-resolution mass spectrometry (LC-HRMS) analysis results were acquired from Agilent 1100 LC/MSD Trap Spectrometer. The FT-IR spectra were recorded by Bruker ALPHA spectrometer (KBr pellets). A STA 449 F3 thermogravimetric/differential thermal analyzer was used to perform TG-DSC tests at  $\text{N}_2$  atmosphere with a heating rate of  $10\text{ }^\circ\text{C min}^{-1}$ . The morphology characterizations were carried out on scanning electron microscope (ZEISS Gemini 300). X-ray photoelectron spectroscopy (XPS) was collected on a Thermo Fisher Esca Lab 250Xi using a monochromic Al X-ray source ( $h\nu = 1486.6\text{ eV}$ ) at Shiyanjia lab ([www.Shiyanjia.com](http://www.Shiyanjia.com)). EPR spectra was carried out on Bruker A300.

### **Electrochemical measurements**

The QAPs electrode was prepared by casting the mixture of QAPs powders, super P conductive additive and polyvinylidene fluoride (PVDF) binder with a weight ratio of 5:4:1 in anhydrous N-methyl-2-pyrrolidinone (NMP) on Cu foil. The film was dried at  $80\text{ }^\circ\text{C}$  for 12 h under vacuum and the average areal mass loading of QAPs was  $1.0\sim 2.0\text{ mg cm}^{-2}$ . The 2032 type coin cells were assembled in an Ar-filled glove box with low level of  $\text{H}_2\text{O}$  ( $< 0.1\text{ ppm}$ ) and  $\text{O}_2$  ( $< 1.0\text{ ppm}$ ) by using 1 M  $\text{NaPF}_6$  in DME, Glass fiber membrane (Whatman, GF/B) and Na metal as electrolyte, separator and anode, respectively. After storing 10 h for rest, the electrochemical performance of these coin cells was evaluated on the LAND CT2001A battery testing system (Wuhan, China) at room temperature. The cyclic voltammetry measurements and the electrochemical impedance spectroscopy (EIS) (frequency range:  $1.0\text{ MHz}\sim 5\text{ mHz}$ ) were completed on the BioLogic VMP3 potentiostat. For all the ex situ characterizations, the samples were prepared by disassembling the cells in an Ar-filled glovebox, and these electrodes were washed by DME and dried in vacuum for further tests. For the assembly of full cell, after precycling in half cells, the  $\text{Na}_3\text{V}_2(\text{PO}_4)_3$  cathode and QAPs anode were paired up in a standard coin cell with the cathode to anode mass ratio of about 5. The current density and capacity were calculated according to the mass of QAPs anode.

## Electronic structure calculation

The crystal simulation was performed with the projected augmented wave (PAW) implementation of density functional theory (DFT) in the Vienna Ab initio Simulation Package (VASP).<sup>5, 6</sup> The generalized gradient approximation (GGA) within Perdew-Burke-Ernzerhof (PBE) form was adopted to describe the exchange-correlation effect.<sup>7</sup> Semiempirical DFT-D3 correction via Grimme's scheme was considered for the long-range van der Waals interactions.<sup>8</sup> The cutoff energy for plane-wave expansion was taken as 500 eV. The k-point sampling of Brillouin zone was performed by using a Monkhorst-Pack grid of  $2 \times 1 \times 7$ .<sup>9</sup> All geometries were relaxed under the convergence criterion of  $10^{-5}$  eV for total energy and 0.02 eV/Å for the Hellmann-Feynman force on each atom.

The Na-ion storage process in QAPs was simulated using the B3LYP functional<sup>10, 11</sup>, implemented in Gaussian 16.<sup>12</sup> The 6-311G(d, p) basis set<sup>13, 14</sup> are adopted for H, C, N, O and Na atoms. The solvent effect of DME was considered by using polarizable continuum model (PCM).

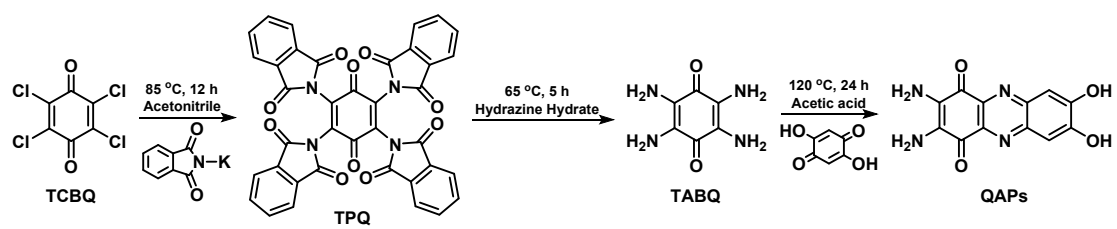


**Fig. S1** Synthetic route of QAPs.

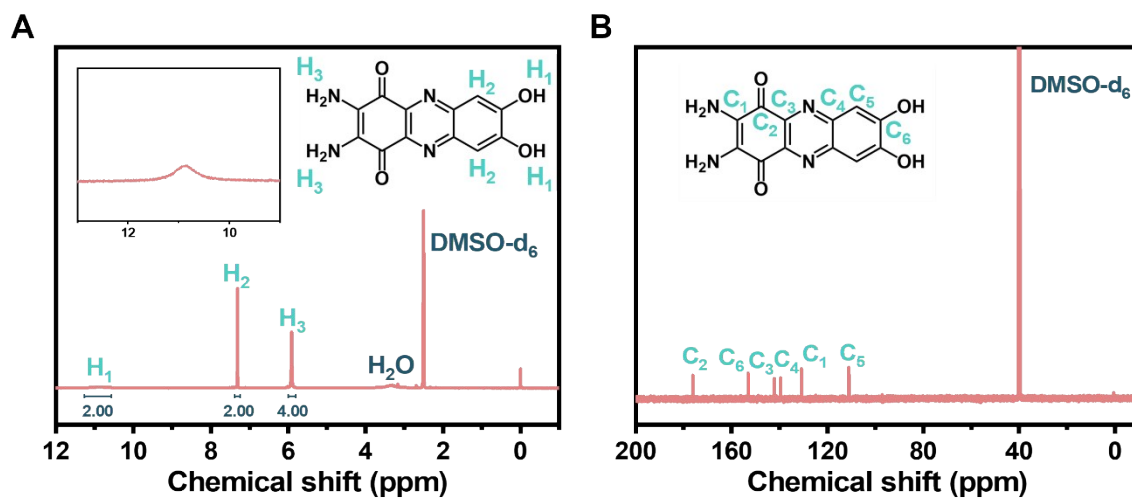


**Fig. S2** Characterization of QAPs. (A)  $^1\text{H}$  NMR spectrum. (B)  $^{13}\text{C}$  NMR spectrum.

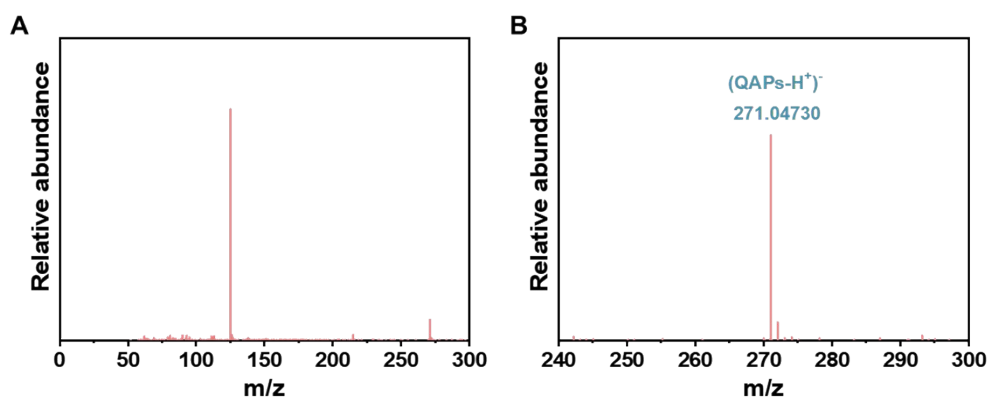


**Fig. S3** HRMS spectrum of QAPs. (A) The full spectrum. Wherein, the strongest absorption peak was the fragment of QAPs. (B) The zoomed-in spectrum.

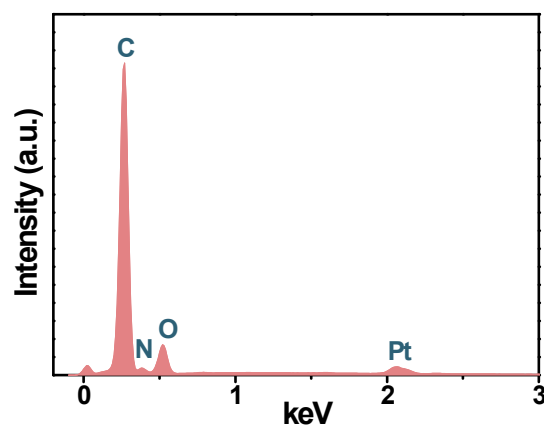


**Fig. S4** The energy dispersive X-ray spectrum showing the composition of QAPs containing C, O and N.



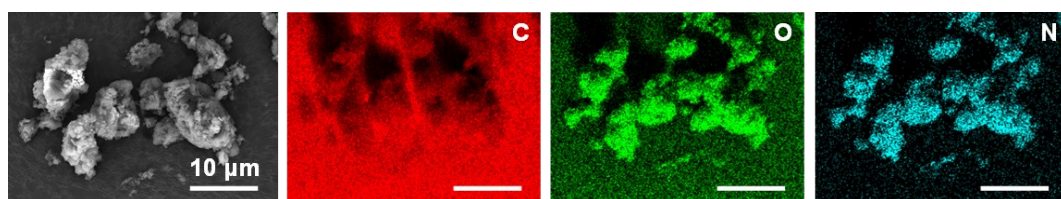


**Fig. S5** The energy dispersive X-ray mapping of QAPs, revealing uniform distribution of C, O and N. Scale bars, 10  $\mu\text{m}$ .

**Table S1** Elemental analyses results of QAPs powders. C, H and N elements were measured by Vario Micro Cube Elemental Analyzer and O was calculated accordingly.

Weight ratio	C%	H%	N%	O%
Theoretical results (QAPs)	52.95	2.96	20.58	23.51
Theoretical results (QAPs•H <sub>2</sub> O)	49.66	3.47	19.30	27.57
Experimental results	50.13	3.33	19.05	27.49

Note: The EA results indicated that water were present in the powders.

**Table S2** Atomic coordinates of QAPs after final Rietveld refinement.

Space group: $P2_1/c$			
$a = 3.6853 \text{ \AA}, b = 27.8881 \text{ \AA}, c = 10.8065 \text{ \AA}$			
$\alpha = 90.00^\circ, \beta = 104.19^\circ, \gamma = 90.00^\circ$			
Atom	$x/a$	$y/b$	$z/c$
H	0.34672	0.65711	0.28382
H	-0.42044	0.77723	-0.31937
H	-0.77745	0.75609	-0.44623
H	0.87146	0.63253	0.50951
H	0.94441	0.69417	0.47979
H	0.03972	0.46768	0.30903
H	-0.26267	0.50142	0.09666
H	0.51219	0.54805	0.47627
C	-0.55502	0.70743	-0.29275
C	-0.31407	0.70798	-0.16011
C	-0.75226	0.66532	-0.34299
C	-0.27095	0.6628	-0.0803
C	-0.71139	0.62059	-0.26572
C	-0.4574	0.61928	-0.1327
C	-0.0105	0.62287	0.11305
C	0.21853	0.62329	0.24205
C	-0.18822	0.57835	0.05869
C	-0.1274	0.53537	0.13518
C	0.10542	0.53637	0.26088
C	0.28043	0.58071	0.31402
O	-0.1519	0.74668	-0.11587
O	0.09943	0.58457	-0.31513
O	0.18552	0.49807	0.34322
O	0.50922	0.58048	0.43635
N	0.01782	0.66378	-0.46417
N	-0.57707	0.74884	-0.36251
N	-0.05617	0.6646	0.04101
N	-0.41724	0.5779	-0.06496

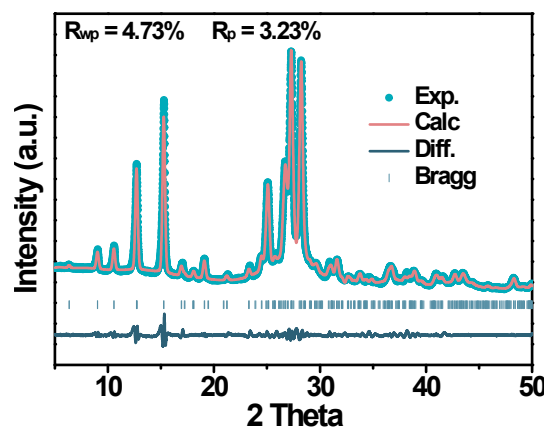


**Fig. S6** Experimental X-ray powder diffraction patterns of QAPs powder compared with the Rietveld-refined profile, showing negligible differences.

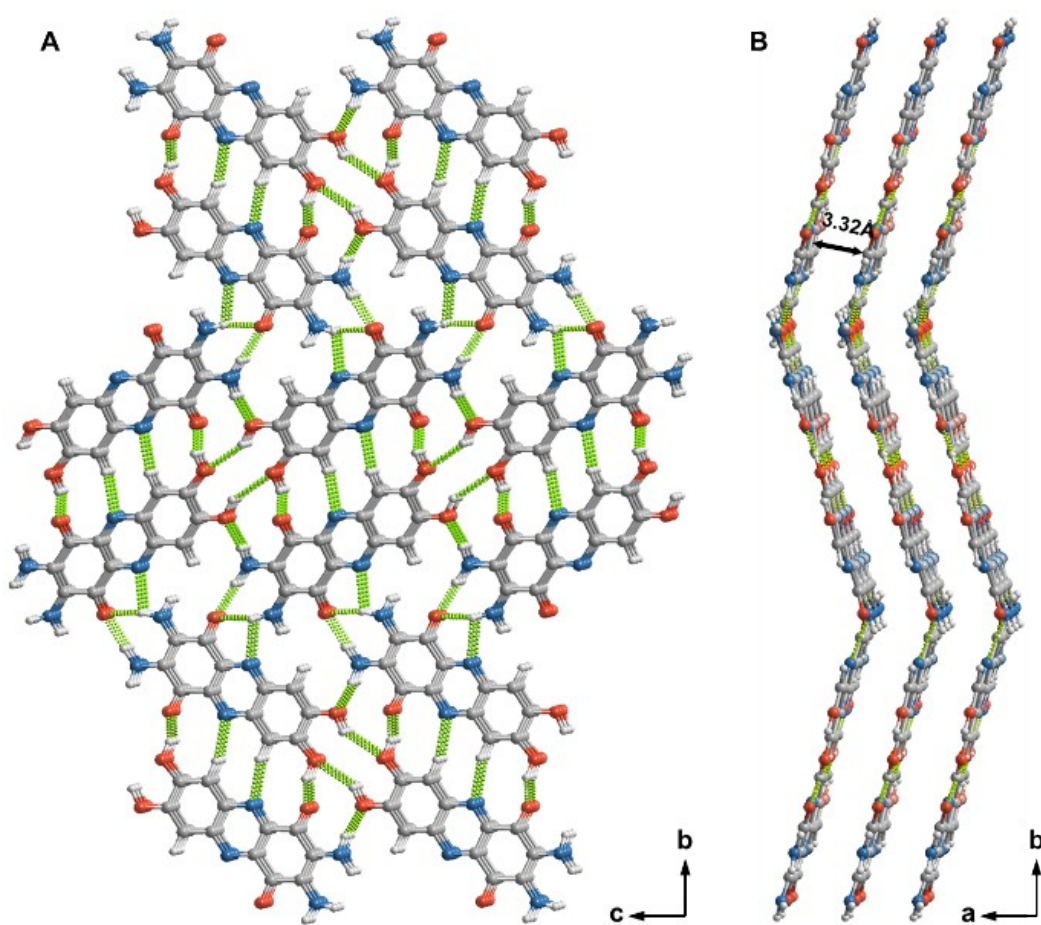


**Fig. S7** Molecular structure of QAPs. (A) Weak intermolecular hydrogen bonds (Green dotted lines) between neighboring QAPs molecules. (B)  $\pi$ - $\pi$  stacking of QAPs.

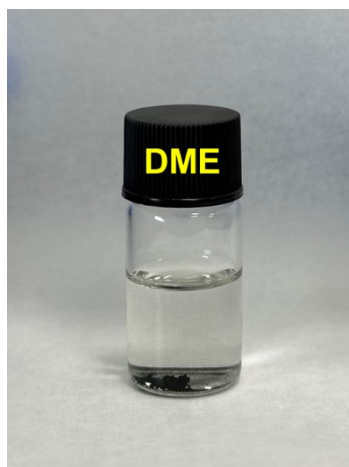


**Fig. S8** The dissolution test of QAPs in DME solvent. The results indicated that QAPs was almost insoluble in DME.

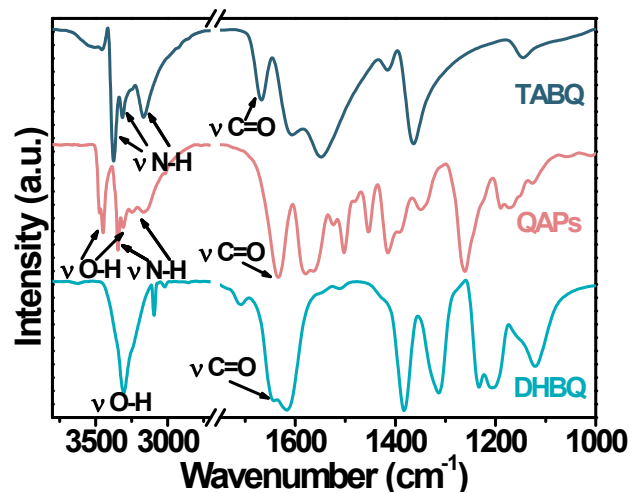


**Fig. S9** The FT-IR spectrum of QAPs, TABQ and DHBQ.

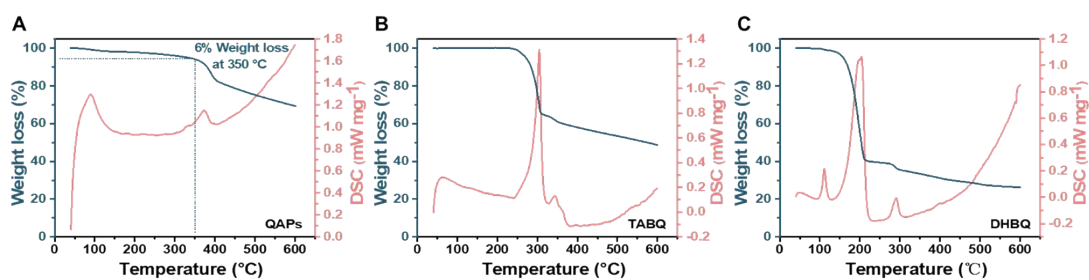


**Fig. S10** The TGA-DSC curves of (A) QAPs, (B) TABQ and (C) DHBQ. QAPs showed high thermal stability. The 6% weight loss could be attributed to the absorbed water, which was coincident well with the EA results (~6.2%). The loss of water started before 100 °C, indicating the water was absorbed water, without strong coordination with the QAPs molecules.



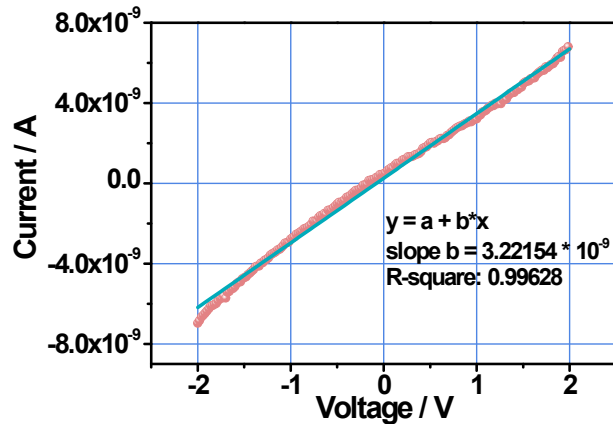


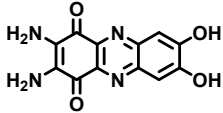
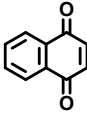
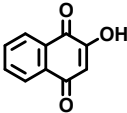
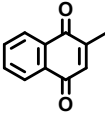
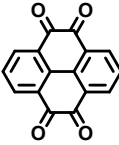
**Fig. S11** I-V curve of QAPs powder.

In order to measure the electrical conductivity of QAPs, the powders of QAPs were pressed into a pellet at the pressure of 20 MPa using a compressed module. The diameter of the obtained pellet is 1.2 cm and the thickness is 1.1 mm. The obtained pellet between two stainless steel chips was pressed tightly to ensure proper electrical contact for test. The electrical conductivity is calculated using the following formula:

$$\sigma = \frac{1}{\rho} = \frac{I}{V} \times \frac{L}{S}$$

Where I and V were the magnitude of the current density and the applied voltage, and S and L were the area and thickness of the pellet, respectively. The electrical conductivity of QAPs is about  $3.31 \times 10^{-10} \text{ S m}^{-1}$ . Considering the grain boundaries and the relative loose structure of the pellet, the real conductivity should be higher.

**Table S3.** The conductivity comparison between the QAPs and other carbonyl small molecules.

Name	Structure	Conductivity (S m <sup>-1</sup> )	Reference
QAPs		$3.31 \times 10^{-10}$	This work
NQ		$2.36 \times 10^{-9}$	15
lawsone		$1.01 \times 10^{-8}$	15
menadione		$8.98 \times 10^{-10}$	15
PTO		$1.47 \times 10^{-11}$	16

Most carbonyl small molecules had such poor electrical conductivity that accurate conductivity couldn't be measured, because the current was already lower than the limit of the test equipment.

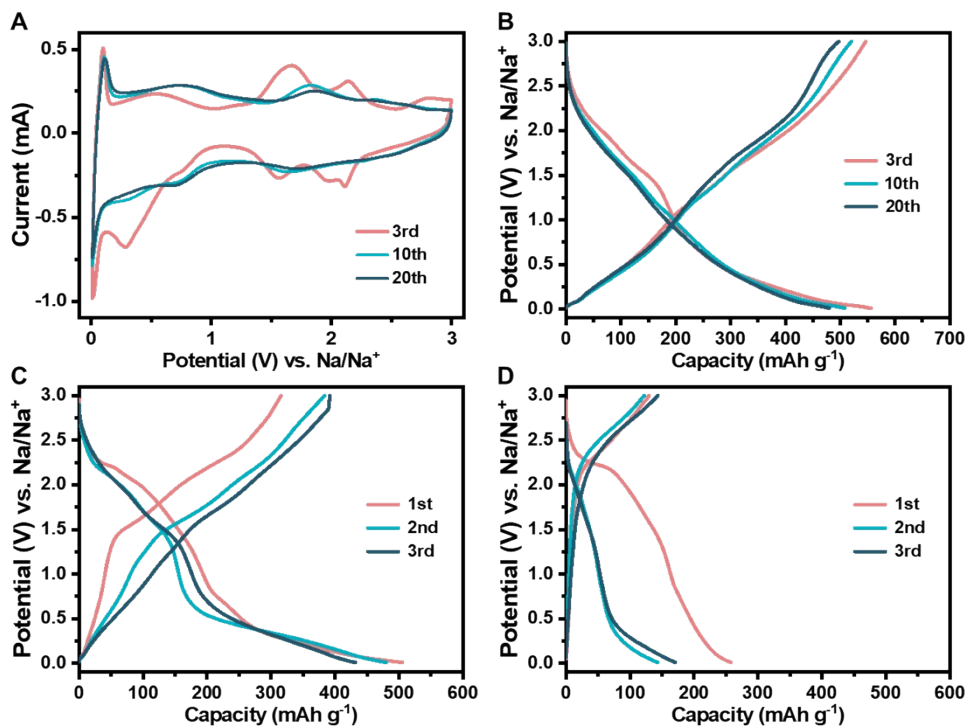


**Fig. S12** Electrochemical performance of QAPs electrodes within a potential window of 0.01-3.0 V (vs. Na/Na<sup>+</sup>). (A) CV curves at 0.5 mV s<sup>-1</sup>, (B) Charge-discharge profiles at 100 mA g<sup>-1</sup>. The weight ratio of active materials, conductive additive and binder was 5:4:1 for (A-B). (C-D) Cycling performance at 0.1 A g<sup>-1</sup> of QAPs with different weight ratio of active materials, conductive additive and binder: (C) 6:3:1, (D) 7:2:1, respectively. The electrochemical performance of QAPs decreased significantly as the ratio of conductive additive decreased.

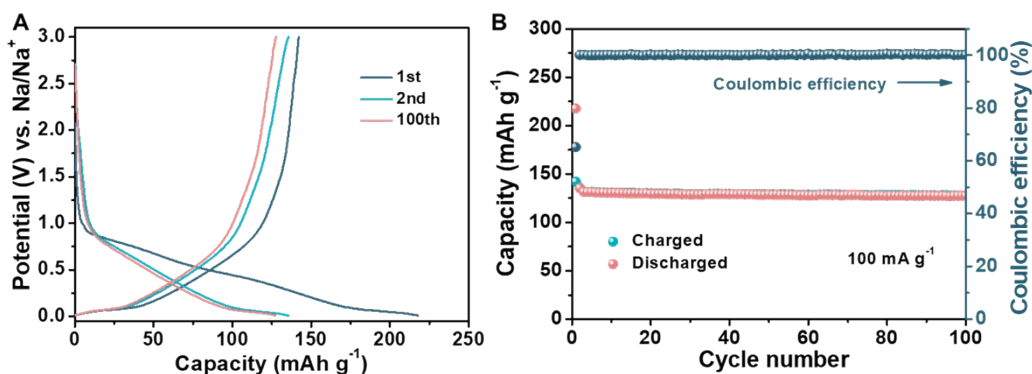


**Fig. S13** Electrochemical performance of super P. (A) Charge-discharge curves and (B) cycling performance of Super P at  $100 \text{ mA g}^{-1}$  within the voltage window of 0.01-3.0 V. The super P electrode was prepared by mixing super P and PVDF at a weight ratio of 9:1. The capacity contribution of QAPs could be ascertained by following equation:

$$C_{QAPs} = C_{test} - \frac{m_{Super P}}{m_{QAPs}} C_{Super P}$$

where  $m$  is the weight of the composition in the electrodes. The capacity of Super P was about  $130 \text{ mAh g}^{-1}$ , indicating the capacity contribution of Super P in the electrodes with composition of 5:4:1 was about  $104 \text{ mAh g}^{-1}$ . The initial capacity of Super P was about  $220 \text{ mAh g}^{-1}$ , indicating the capacity contribution of Super P and formation of SEI in the electrodes with composition of 5:4:1 was about  $176 \text{ mAh g}^{-1}$ .

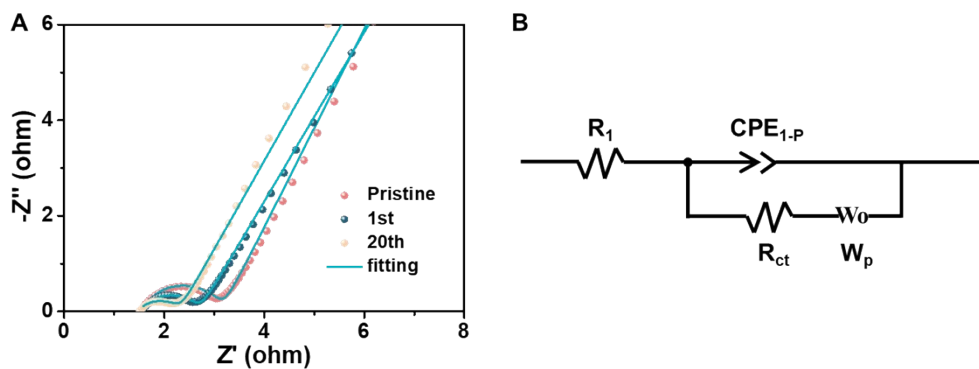


**Fig. S14.** (A) Nyquist plots of QAPs electrode in the pristine, the 1st charging state and the 20th charging state, respectively. (B) The equivalent circuit of QAPs electrode.

**Table S4.** The values of the four elements in the equivalent circuit.

Cycle number	$R_1(\Omega)$	$CPE_{1-P}$	$R_{ct}(\Omega)$	$W_p$
Pristine	1.543	0.738	1.645	0.715
1st	1.511	0.640	1.222	0.673
20th	1.464	0.574	0.888	0.688

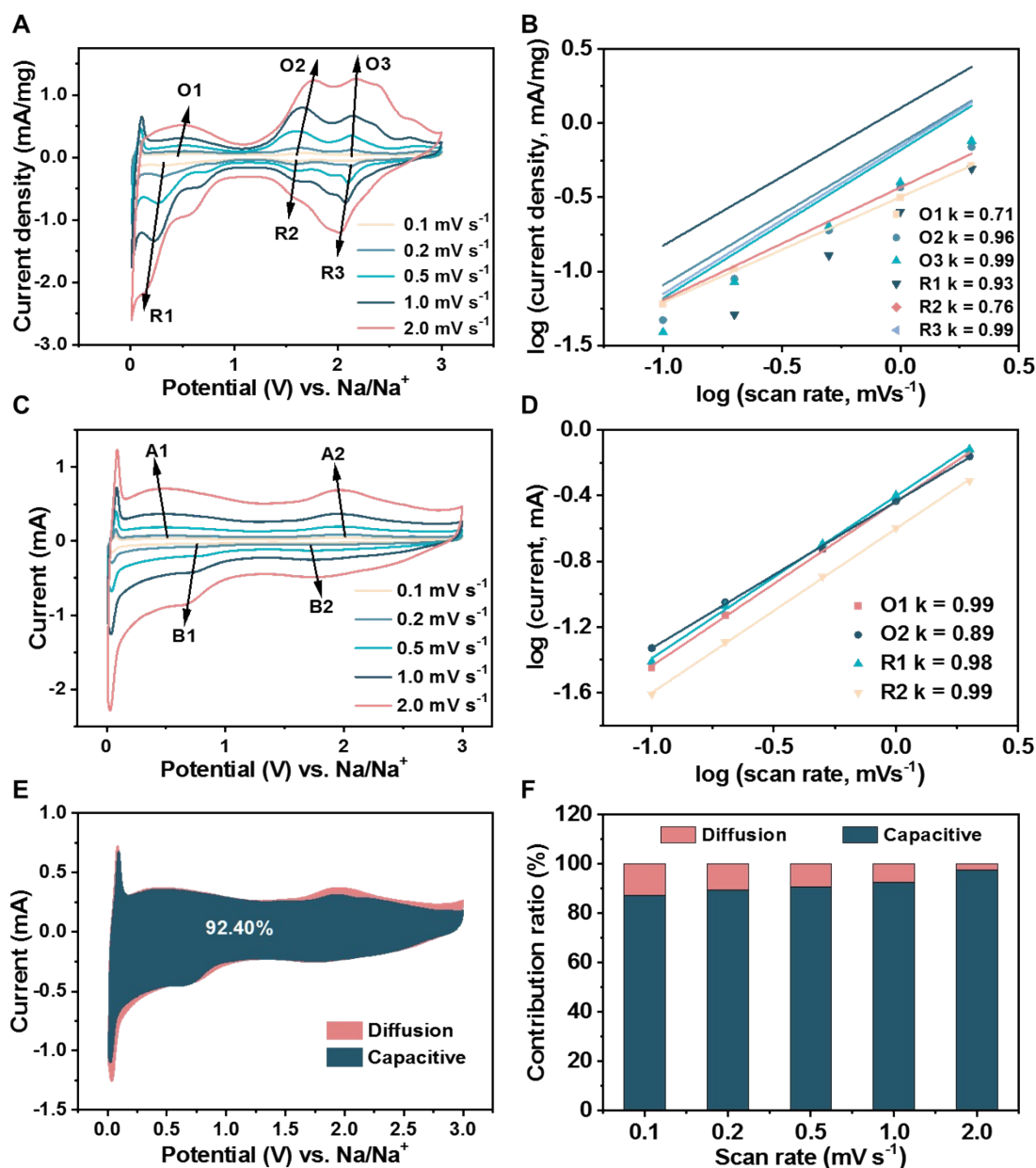


**Fig. S15** Electrochemical kinetic analysis of the QAPs electrode. (A) CV profiles of the second cycle in different samples at different scan rates. (B) The plots of  $\lg$  (peak current density,  $i$ ) vs.  $\lg$  (scan rate,  $v$ ) and the slope  $b$  of the redox peaks corresponding to (A). (C) CV profiles at different scan rates for the same sample after stabilization. (D) The plots of  $\lg$  (peak current,  $i$ ) vs.  $\lg$  (scan rate,  $v$ ) and the slope  $b$  of the redox peaks corresponding to (C). (E) The CV profile with the pseudocapacitive contribution of QAPs electrode at a scan rate of  $1 \text{ mV s}^{-1}$ . (F) The capacitive contributions at various scan rates. The results indicated that the contribution of capacitive process is comparable before and after multiple cycles, with similar slope  $b$ , indicating that the sodium storage mechanism does not change before and after multiple cycles.

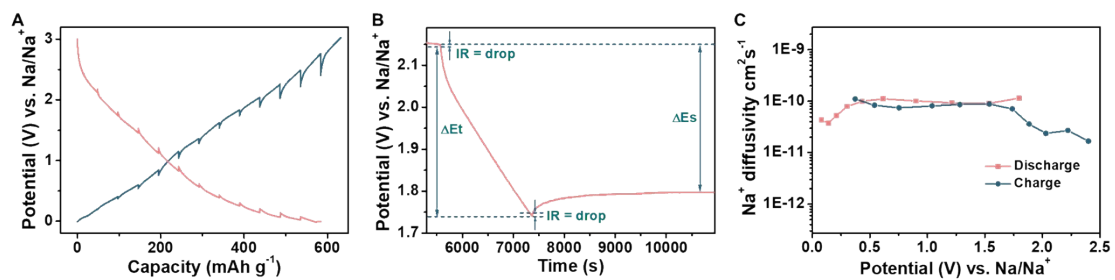


**Fig. S16** (A) Full charge-discharge cycle. (B) A typical step of GITT discharge curve of QAPs in SIBs. (C) The Na<sup>+</sup> diffusion coefficient of QAPs in SIBs.

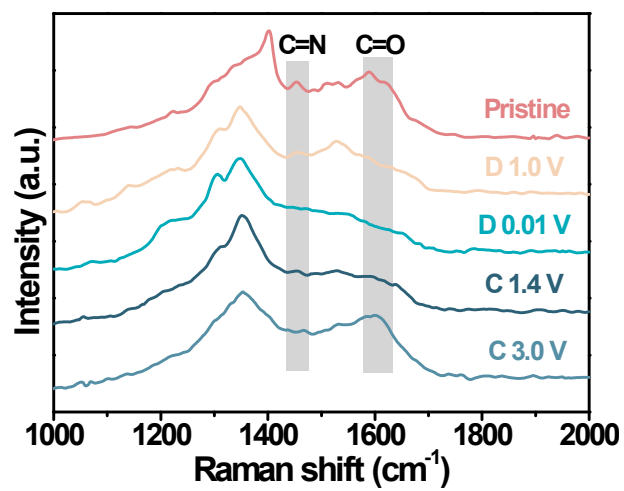


**Fig. S17** Ex situ Raman spectra of QAPs electrodes at different states.



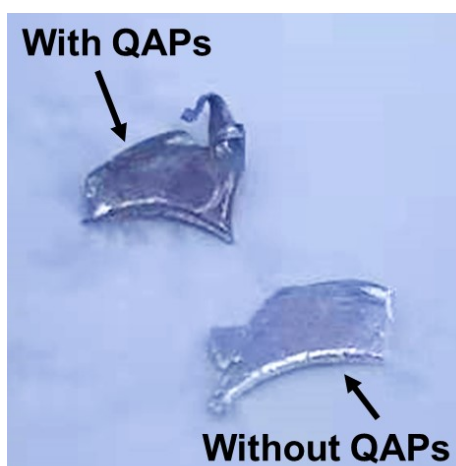


**Fig. S18** The sodium pieces were collected after immersing in the electrolyte (1 M NaPF<sub>6</sub> in DME) with or without QAPs for 10 min in an Ar-filled glove box with low level of H<sub>2</sub>O (< 0.1 ppm) and O<sub>2</sub> (< 1.0 ppm).

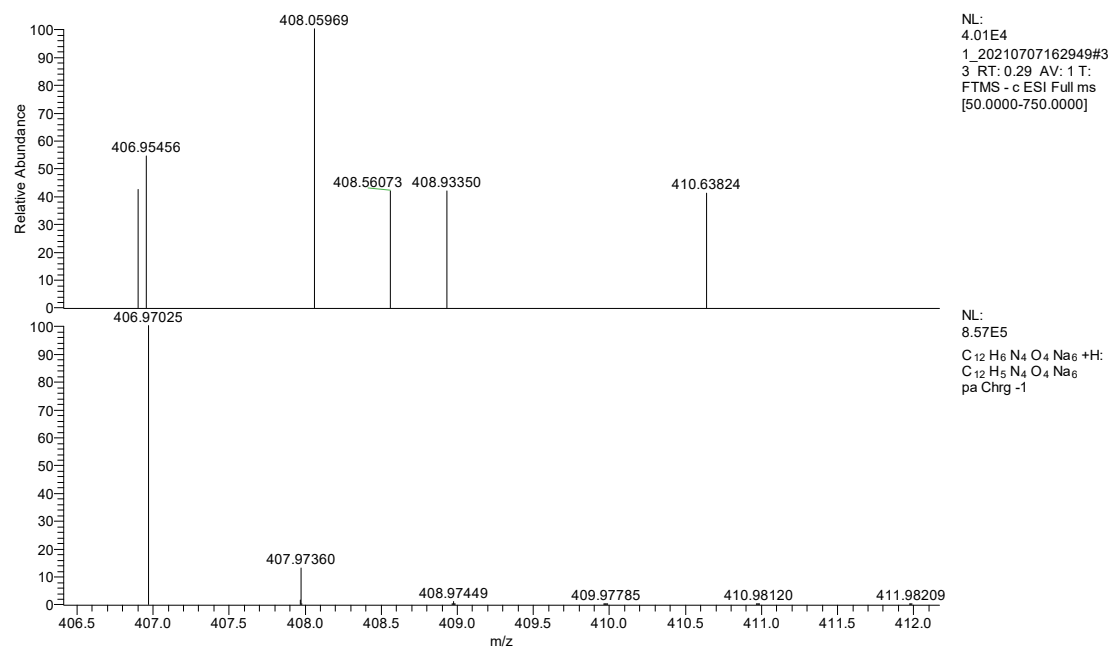


**Fig. S19** The high resolution mass spectrometry of the QAPs electrodes after being discharged to 0.01 V. Top: experimental results, bottom: theoretical results. The results indicated that QAPs indeed could store six Na ions with deprotonation ( $-2 H^+$ ).

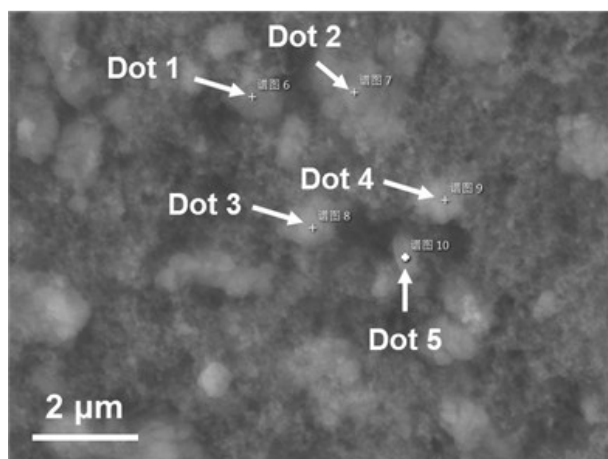


**Fig. S20** The SEM image of the recharged QAPs electrodes (Charged to 3.0 V). These marked dots was detected for energy dispersive X-ray spectra.

**Table S5** The atomic percentage of the recharged QAPs electrodes (Charged to 3.0 V) from energy dispersive X-ray spectra. The slight P elements came from the residual electrolytes ( $\text{NaPF}_6$ ). After deducting the content of sodium ions from the salts, the atomic ratio of sodium ions to nitrogen in the electrode was 1:3.65.

Element	Dot 1	Dot 2	Dot 3	Dot 4	Dot 5	Average
Na	3.46	3.97	3.25	3.07	2.57	3.264
N	11.60	14.59	12.47	10.82	7.96	11.488
P	0.13	0.15	0.13	0.08	0.09	0.116

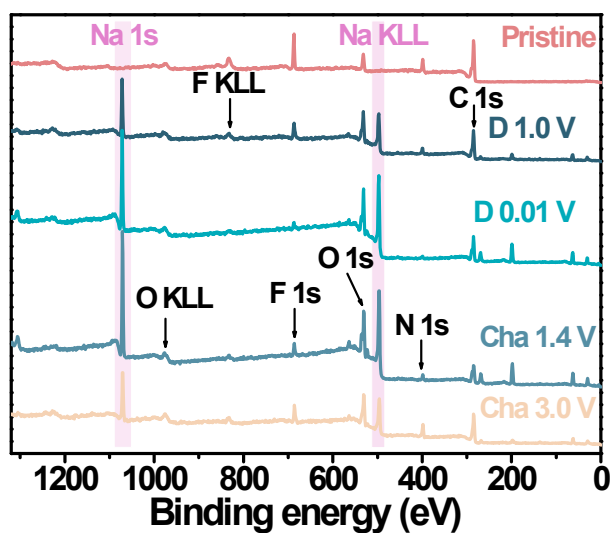


**Fig. S21** The XPS spectra of the QAPs electrodes at different states during the discharge and recharge process.

**Table S6** The atomic percentage of the recharged QAPs electrodes (charged to 3.0 V) from XPS spectra. The slight P elements came from the residual electrolytes ( $\text{NaPF}_6$ ). After deducting the content of sodium ions from the salts, the atomic ratio of sodium ions to nitrogen in the electrode was 1:3.41 and the atomic ratio of sodium ions to oxygen in the electrode was 1:4.65.

Element	C	O	N	Na	P
Atomic%	53.23	23.44	17.21	5.58	0.54

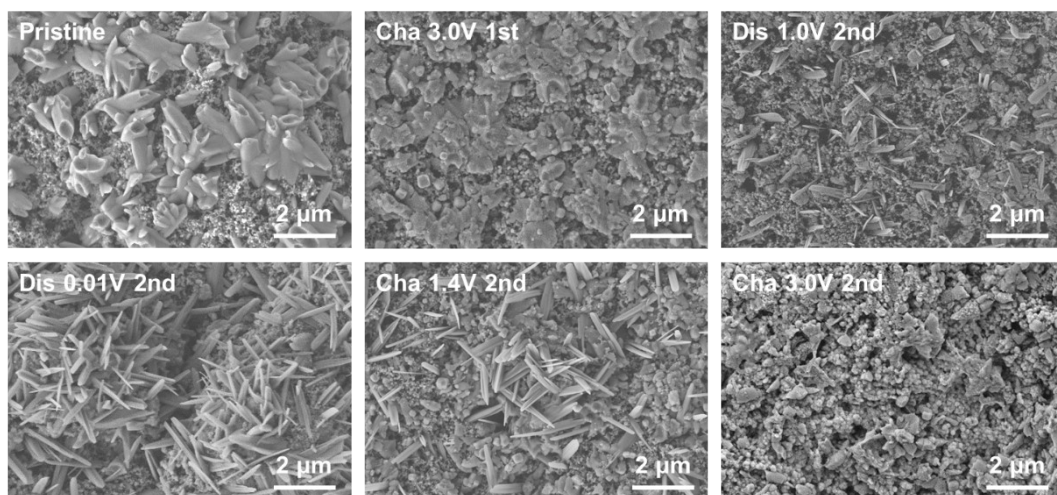


**Fig. S22** SEM images of the QAPs electrodes at different states during the discharge and recharge process. Small blocks rather than the pristine QAPs particles could be observed after recharge, indicating the formation of different materials.

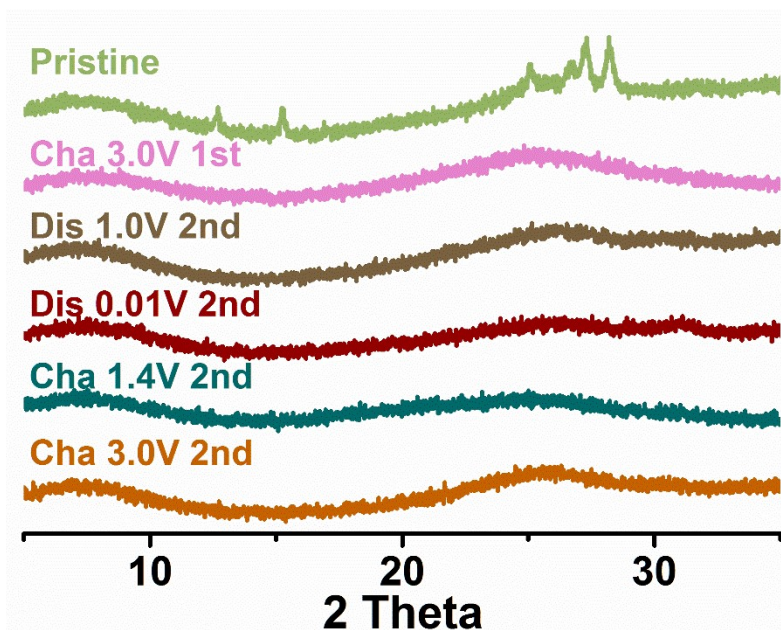


**Fig. S23** The XRD patterns of the QAPs electrodes during cycling. The diffraction peaks disappeared, indicating the destroy of intermolecular hydrogen bonds and leading to amorphous structure.

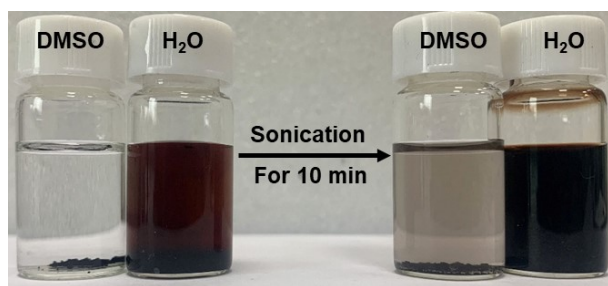


**Fig. S24** The solution stability of as-synthesized QAPs\_2Na\_syn (10 mg) in DMSO (5 mL) and H<sub>2</sub>O (5 mL). It was readily dissolved in the H<sub>2</sub>O while was almost insoluble in DMSO.

**Table S7** Elemental analyses results of QAPs\_2Na\_syn powders. C, H and N elements were measured by Vario Micro Cube Elemental Analyzer, Na element was measured by ICP and O was calculated accordingly.

Weight ratio	C%	H%	N%	Na%	O%
Theoretical results (QAPs_2Na_syn)	45.58	1.91	17.72	14.54	20.24
Theoretical results (QAPs_2Na_syn •2.5H <sub>2</sub> O•0.2NaOH)	39.04	3.06	15.17	13.70	29.03
Experimental results	39.30	2.39	15.20	13.48	29.63

Note: The EA results indicated that water were present in the powders with slight NaOH residuals.



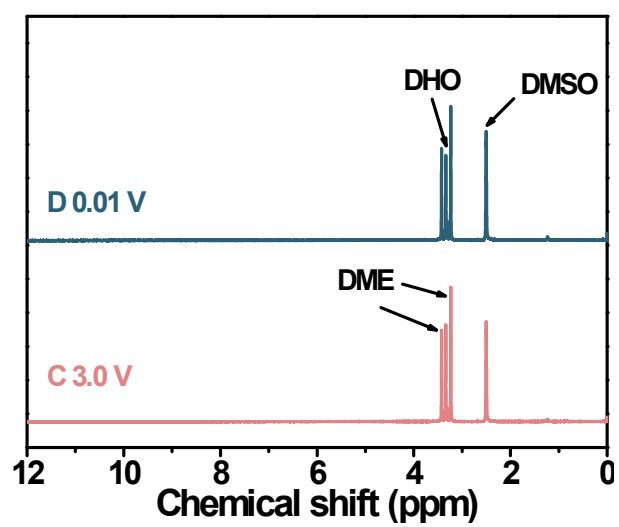


**Fig. S25** The QAPs electrodes after cycle were directly dissolved in Deuterated DMSO for  $^1\text{H}$  NMR spectra.

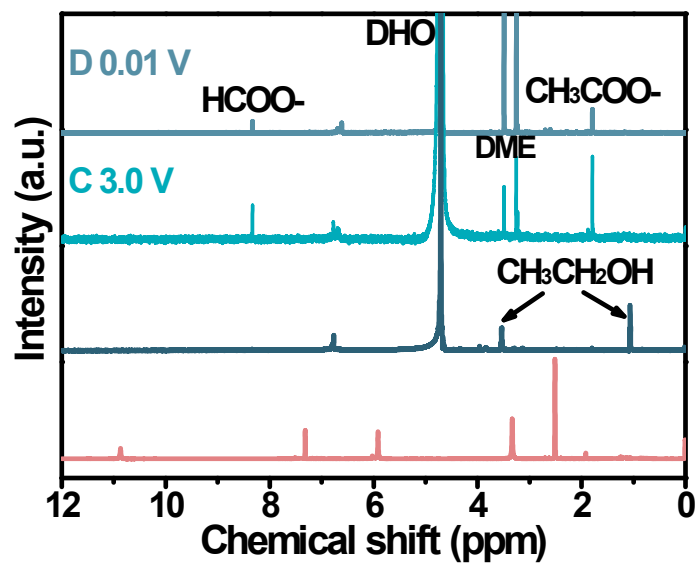


**Fig. S26** The <sup>1</sup>H NMR spectra of QAPs, QAPs\_2Na\_syn, the charged QAPs electrodes at 3.0 V and the discharged QAPs electrodes at 0.01 V. QAPs electrodes and QAPs\_2Na\_syn were dissolved in D<sub>2</sub>O for test. Active hydrogen could not be observed due to the use of D<sub>2</sub>O. The HCOO<sup>-</sup> and CH<sub>3</sub>COO<sup>-</sup> signals could be ascribed to the formed SEI. The QAPs were measured in DMSO-d<sub>6</sub>. Compared with the <sup>1</sup>H NMR spectrum of QAPs, the chemical shift of the hydrogen atoms in QAPs electrodes and QAPs\_2Na\_syn shifted up-field (low chemical shift), which should be ascribed to the electron donating effect of the phenolate (-ONa).

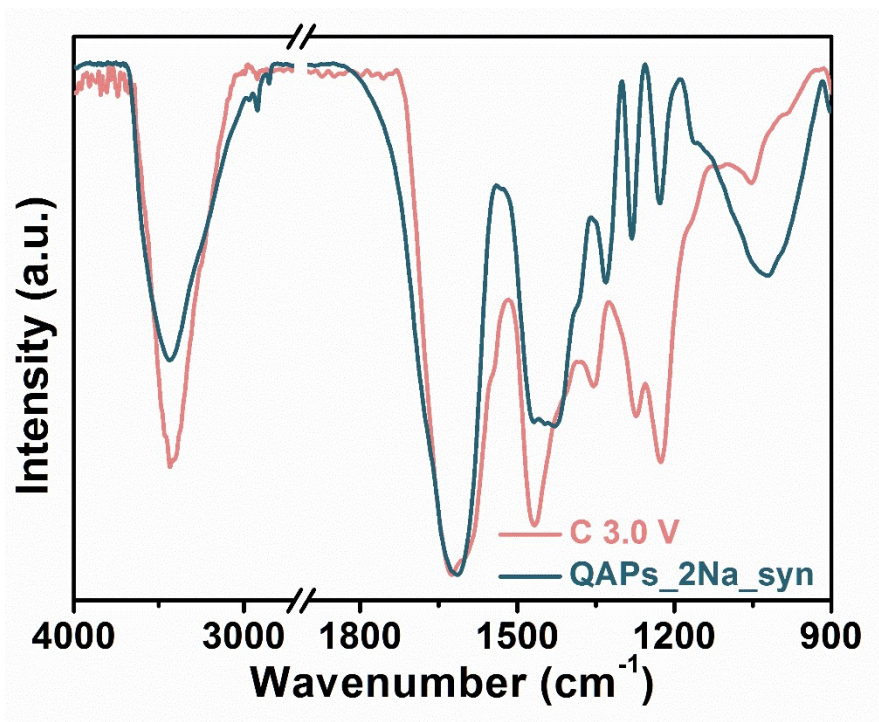


**Fig. S27** The FT-IR spectrum of the as-synthesized QAPs\_2Na\_syn and the recharged QAPs electrodes at 3.0 V.

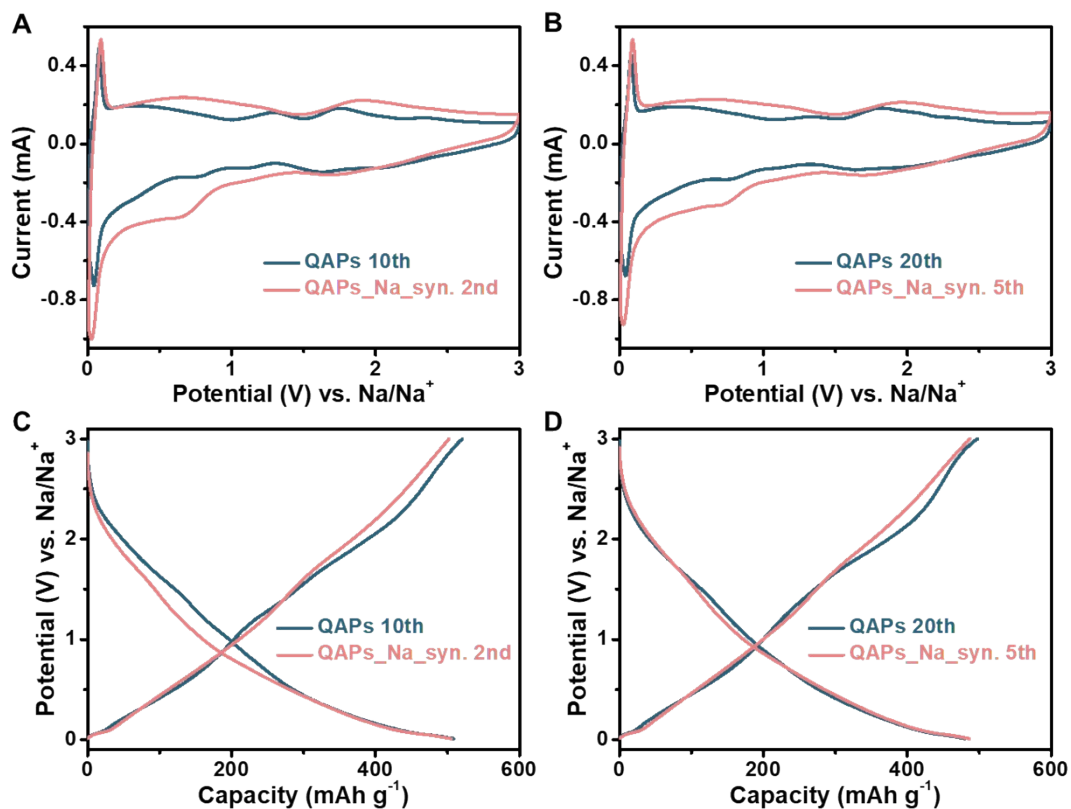


**Fig. S28** The comparison of electrochemical properties between QAPs electrodes and QAPs<sub>2Na\_syn</sub> electrodes. (A, B) The CV curves of QAPs electrodes and QAPs<sub>2Na\_syn</sub> electrodes after several cycles at a scan rate of 0.5 mV s<sup>-1</sup>. (C, D) The galvanostatic charge/discharge profiles of QAPs electrodes and QAPs<sub>2Na\_syn</sub> electrodes after several cycles at 100 mA g<sup>-1</sup>.

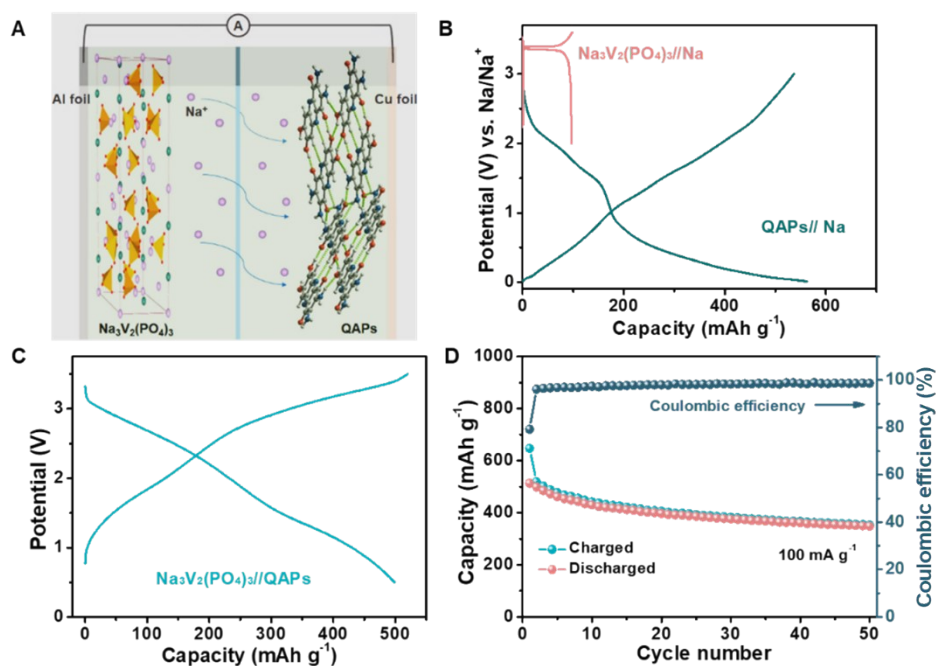


**Fig. S29** Electrochemical performance of the full cells assembled with  $\text{Na}_3\text{V}_2(\text{PO}_4)_3$  cathode and QAPs anode. (A) Schematic diagram of full cells. (B) Charge-discharge curves of  $\text{Na}_3\text{V}_2(\text{PO}_4)_3//\text{Na}$  half-cells and  $\text{QAPs}//\text{Na}$  half-cells at  $100 \text{ mA g}^{-1}$ . (C) The second charge-discharge curve of  $\text{Na}_3\text{V}_2(\text{PO}_4)_3//\text{QAPs}$  full cells at  $100 \text{ mA g}^{-1}$ . (D) Cycling performance of  $\text{Na}_3\text{V}_2(\text{PO}_4)_3//\text{QAPs}$  full cells at  $100 \text{ mA g}^{-1}$ .

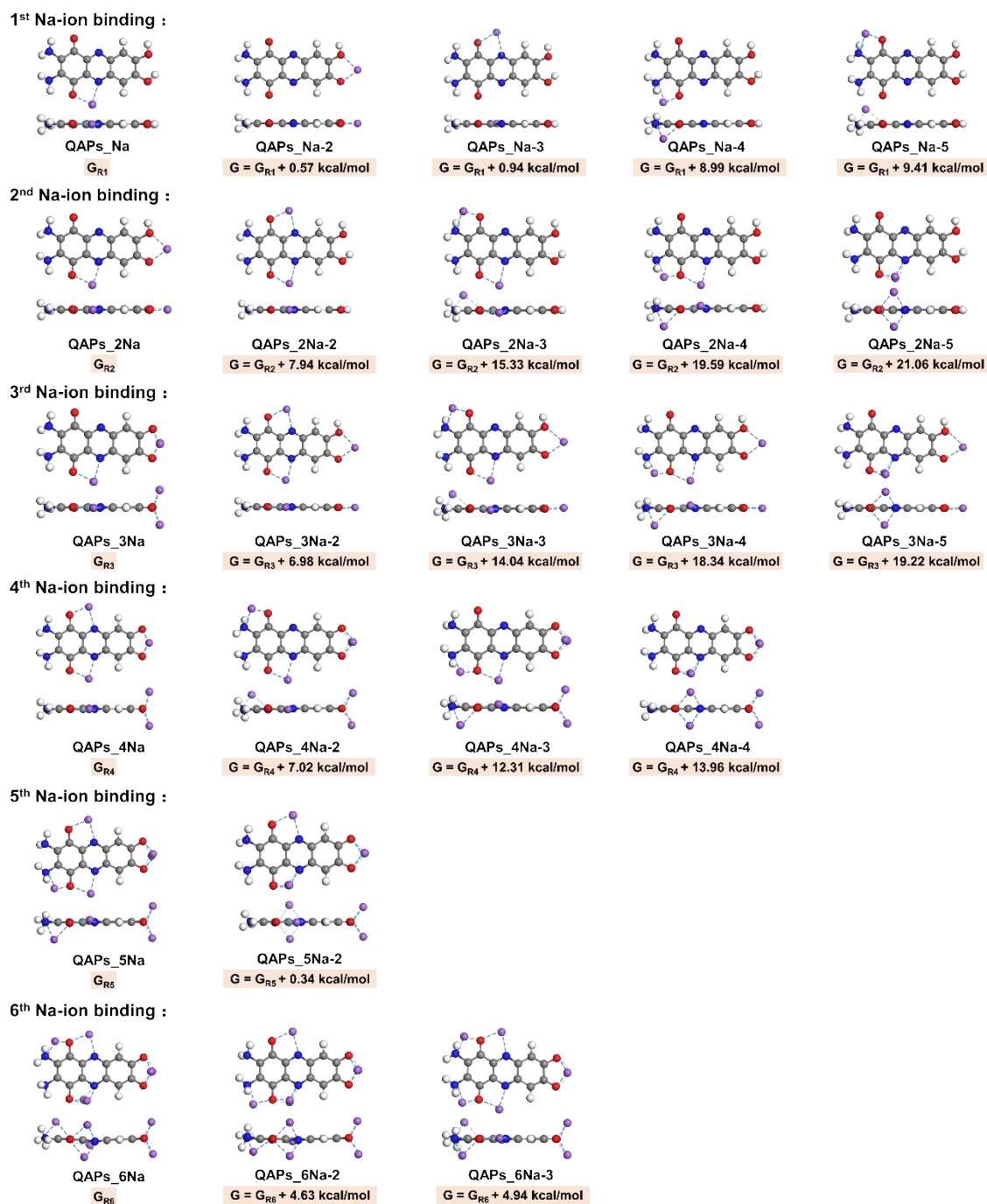


**Fig. S30** Comparison of possible structures for QAPs<sub>x</sub>Na (x = 1, 2, 3, 4, 5, 6) during the sodiation process. Where QAPs<sub>Na</sub>, QAPs<sub>2Na</sub>, QAPs<sub>3Na</sub>, QAPs<sub>4Na</sub>, QAPs<sub>5Na</sub> and QAPs<sub>6Na</sub> are the most stable structures while other structures have higher relative energies, indicating less possibility to exist during Na-ion storage.

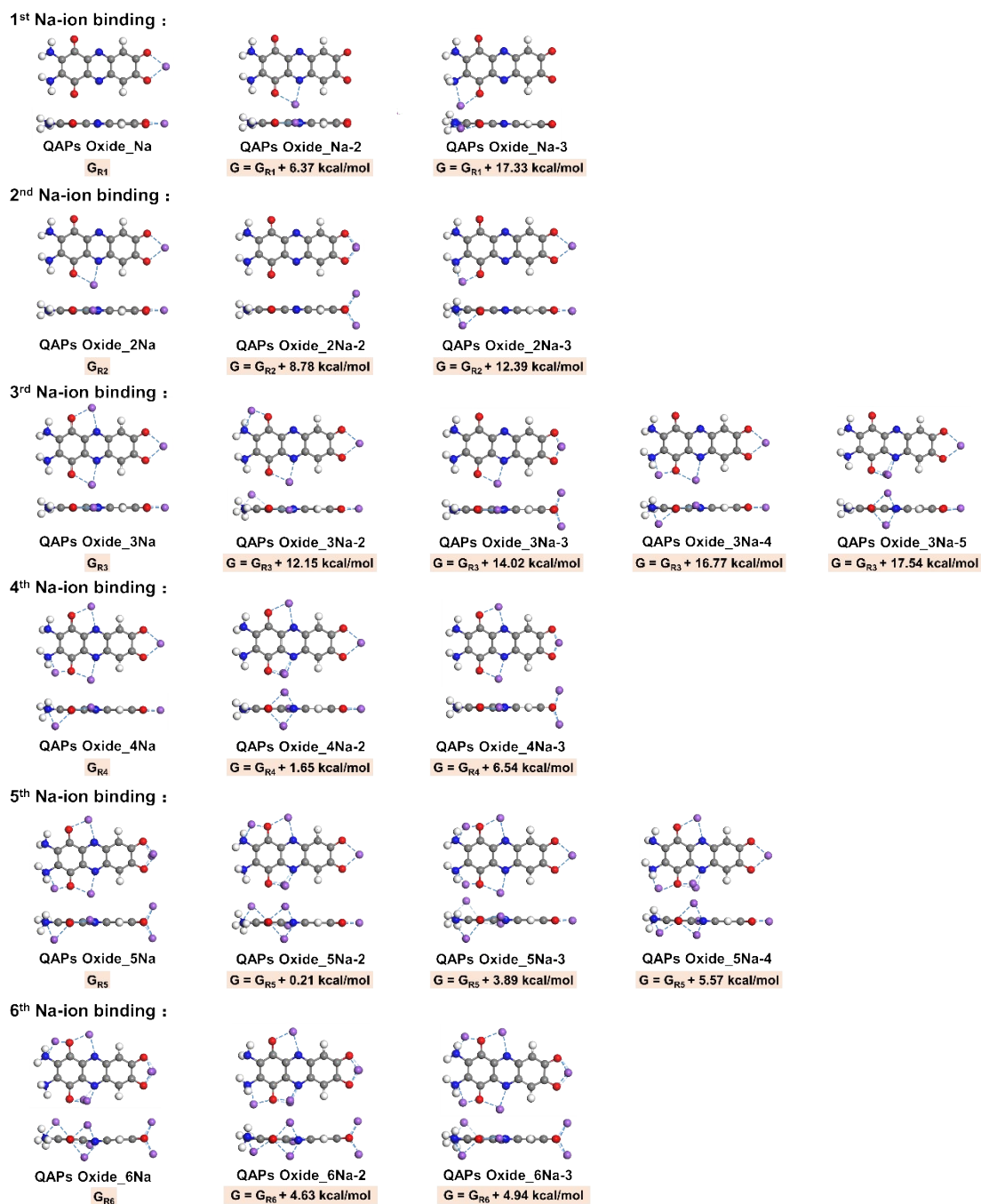


**Fig. S31** Comparison of possible structures for QAPs oxide\_xNa ( $x = 1, 2, 3, 4, 5, 6$ ) during the sodiation process. Where QAPs oxide\_Na, QAPs oxide\_2Na, QAPs oxide\_3Na, QAPs oxide\_4Na, QAPs oxide\_5Na and QAPs oxide\_6Na are the most stable structures while other structures have higher relative energies, indicating less possibility to exist during Na-ion storage. Noted that QAPs oxide\_5Na and QAPs oxide\_6Na were equal to QAPs\_5Na and QAPs\_6Na, respectively.

**Table S8** The Gibbs free energies of these various QAPs\_xNa and QAPs Oxide\_xNa compounds.

Structure	Spin State	Gibbs free energy (Hartree)
QAPs	singlet	-982.1166
QAPs_1Na	doublet	-1144.5130
QAPs_2Na	singlet	-1306.3123
QAPs_3Na	doublet	-1468.1038
QAPs_4Na	singlet	-1630.4713
QAPs_5Na	doublet	-1792.8029
QAPs_6Na	singlet	-1955.1127
QAPs Oxide	singlet	-980.8665
QAPs Oxide_1Na	doublet	-1143.3119
QAPs Oxide_2Na	singlet	-1305.7318
QAPs Oxide_3Na	doublet	-1468.1262
QAPs Oxide_4Na	singlet	-1630.4817
QAPs Oxide_5Na	doublet	-1792.8029
QAPs Oxide_6Na	singlet	-1955.1127

$G_{\text{Na}} = -162.3087$  Hartree,  $G_{\text{H}_2} = -1.1811$  Hartree.



**Table S9** The calculated reduction potentials at the B3LYP/6-31+G(d, p) level in DME solvent.

Reaction Process	Redox Potential (V)
QAPs+Na <sup>+</sup> +e <sup>-</sup> → QAPs_Na	2.38
QAPs_Na+Na <sup>+</sup> +e <sup>-</sup> → QAPs_2Na +1/2H <sub>2</sub>	2.21
QAPs_2Na+Na <sup>+</sup> +e <sup>-</sup> → QAPs_3Na +1/2H <sub>2</sub>	2.00
QAPs_3Na+Na <sup>+</sup> +e <sup>-</sup> → QAPs_4Na	1.60
QAPs_4Na+Na <sup>+</sup> +e <sup>-</sup> → QAPs_5Na	0.62
QAPs_5Na+Na <sup>+</sup> +e <sup>-</sup> → QAPs_6Na	0.03

**Table S10** The calculated redox potentials at the B3LYP/6-31+G(d, p) level in DME solvent.

Reaction Process	Redox Potential (V)
QAPs oxide+Na <sup>+</sup> +e <sup>-</sup> →QAPs oxide_Na	3.72
QAPs oxide_Na+Na <sup>+</sup> +e <sup>-</sup> →QAPs oxide_2Na	3.03
QAPs oxide_2Na+Na <sup>+</sup> +e <sup>-</sup> →QAPs oxide_3Na	2.33
QAPs oxide_3Na+Na <sup>+</sup> +e <sup>-</sup> → QAPs oxide_4Na	1.28
QAPs oxide_4Na+Na <sup>+</sup> +e <sup>-</sup> → QAPs oxide_5Na	0.34
QAPs oxide_5Na+Na <sup>+</sup> +e <sup>-</sup> → QAPs oxide_6Na	0.03

The theoretical reduction potential of (V vs. Na<sup>+</sup>/Na) QAPs molecule is calculated using the formulas:

$$E_{\text{redox}} = -\Delta G/nF$$

$$= -(G_{\text{final}} - G_{\text{initial}} - G_{\text{Na}} + m/2G_{\text{H}_2})/nF$$

where  $E_{\text{redox}}$  is the redox potential of specified step,  $G_{\text{final}}$ ,  $G_{\text{initial}}$ ,  $G_{\text{Na}}$  and  $G_{\text{H}_2}$  are the calculated Gibbs free energies of the final and initial QAPs during the sodiation, sodium atom and hydrogen molecule, respectively; m and n represent the number of protons escaped and the number of electrons transferred during the step respectively, and F is the Faraday constant.

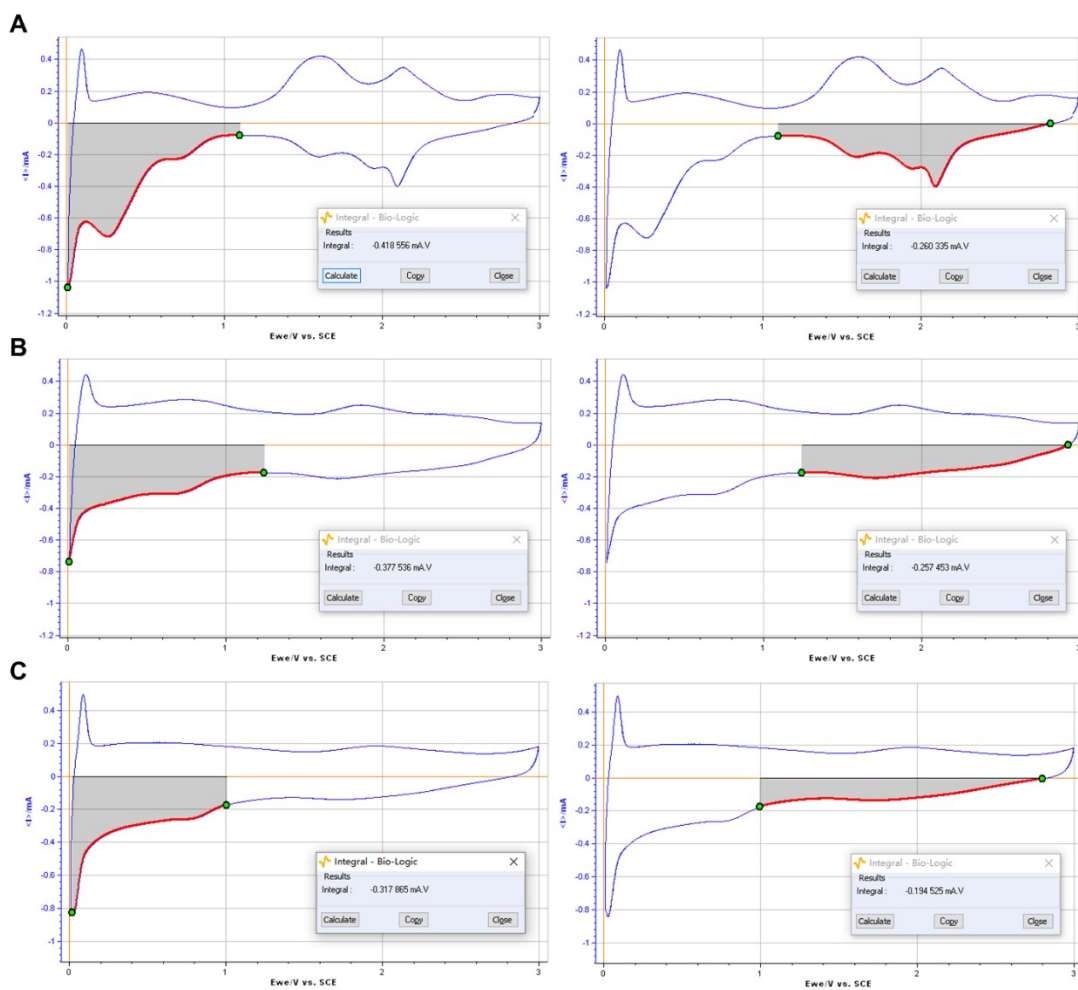


**Fig. S32** The integral areas for the redox peaks of (A) the second cycle of QAPs electrode, (B) the 20th cycle of QAPs electrode, and (C) the 20th cycle of QAPs\_2Na\_syn electrode. All three electrodes showed an integral areas ratio of around 3:2 for the two parts in the CV curves, indicating that 2-electrons transfer at voltages about 2 V and 3-electrons transfer at voltages lower than 1.2 V.

## References

1. S. F. Xu, H. Y. Li, Y. Chen, Y. C. Wu, C. Jiang, E. J. Wang and C. L. Wang, *J. Mater. Chem. A*, 2020, **8**, 23851-23856.
2. Y. Chen, H. Li, M. Tang, S. Zhuo, Y. Wu, E. Wang, S. Wang, C. Wang and W. Hu, *J. Mater. Chem. A*, 2019, **7**, 20891-20898.
3. Z. Luo, L. Liu, J. Ning, K. Lei, Y. Lu, F. Li and J. Chen, *Angew. Chem. Int. Ed.*, 2018, **57**, 9443-9446.
4. M. R. Tuttle, S. T. Davis and S. Zhang, *ACS Energy Lett.*, 2021, **6**, 643-649.
5. G. Kresse and J. Furthmuller, *Phys. Rev. B*, 1996, **54**, 11169-11186.
6. P. E. Blochl, *Phys. Rev. B*, 1994, **50**, 17953-17979.
7. J. P. Perdew, K. Burke and M. Ernzerhof, *Phys. Rev. Lett.*, 1996, **77**, 3865-3868.
8. S. Grimme, *J. Comput. Chem.*, 2006, **27**, 1787-1799.
9. H. J. Monkhorst and J. D. Pack, *Phys. Rev. B*, 1976, **13**, 5188-5192.
10. A. D. Becke, *J. Chem. Phys.*, 1993, **98**, 5648-5652.
11. C. Lee, W. Yang and R. G. Parr, *Phys. Rev. B*, 1988, **37**, 785-789.
12. Gaussian 16, Revision C.01, M. J. Frisch, G. W. Trucks, H. B. Schlegel, G. E. Scuseria, M. A. Robb, J. R. Cheeseman, G. Scalmani, V. Barone, G. A. Petersson, H. Nakatsuji, X. Li, M. Caricato, A. V. Marenich, J. Bloino, B. G. Janesko, R. Gomperts, B. Mennucci, H. P. Hratchian, J. V. Ortiz, A. F. Izmaylov, J. L. Sonnenberg, D. Williams-Young, F. Ding, F. Lipparini, F. Egidi, J. Goings, B. Peng, A. Petrone, T. Henderson, D. Ranasinghe, V. G. Zakrzewski, J. Gao, N. Rega, G. Zheng, W. Liang, M. Hada, M. Ehara, K. Toyota, R. Fukuda, J. Hasegawa, M. Ishida, T. Nakajima, Y. Honda, O. Kitao, H. Nakai, T. Vreven, K. Throssell, J. A. Montgomery, Jr., J. E. Peralta, F. Ogliaro, M. J. Bearpark, J. J. Heyd, E. N. Brothers, K. N. Kudin, V. N. Staroverov, T. A. Keith, R. Kobayashi, J. Normand, K. Raghavachari, A. P. Rendell, J. C. Burant, S. S. Iyengar, J. Tomasi, M. Cossi, J. M. Millam, M. Klene, C. Adamo, R. Cammi, J. W. Ochterski, R. L. Martin, K. Morokuma, O. Farkas, J. B. Foresman, and D. J. Fox, Gaussian, Inc., Wallingford CT, 2016.
13. W. J. Hehre, R. Ditchfield and J. A. Pople, *J. Chem. Phys.*, 1972, **56**, 2257-2261.
14. M. M. Francl, W. J. Pietro, W. J. Hehre, J. S. Binkley, M. S. Gordon, D. J. DeFrees and J. A. Pople, *J. Chem. Phys.*, 1982, **77**, 3654-3665.
15. J. Lee and M. J. Park, *Adv. Energy Mater.*, 2017, **7**, 1602279.
16. H. Dong, O. Tutusaus, Y. Liang, Y. Zhang, Z. Lebens-Higgins, W. Yang, R. Mohtadi and Y. Yao, *Nature Energy*, 2020, **5**, 1043-1050.